Photocatalytic C-O activation and biomass derived polymer precursor production with CO_2 over redox centers spatially separated Sv-ZnIn$_2$S$_4$/BiVO$_4$

Meilin Sheng , Chuan Gan , Yue Li , Zujie Hu , Qian Zhou , Long Qin , Jianmin Ren , Heyan Jiang [*]

Key Laboratory of Catalysis Science and Technology of Chongqing Education Commission, Chongqing Key Laboratory of Catalysis and New Environmental Materials, Chongqing Technology and Business University, Chongqing 400067, PR China

ABSTRACT

It is a very important, promising and challenging exploration to achieve the CO_2 transformation and renewable biomass utilization for value added chemical intermediate production. Herein, S vacancies enriched Z-scheme Sv-ZnIn$_2$S$_4$/BiVO$_4$ was designed to achieve photocatalytic C-O activation and carboxylation with CO_2 in the absence of sacrificial agent. Various aromatic alcohols could be utilized to prepare corresponding carbon chain increased aryl carboxylic acids through acetic anhydride assisted esterification, photogenerated holes oxidization induced benzyl radical generation and subsequent CO_2 carboxylation. It is worth mentioning that furfuryl alcohol could also achieve the C-O activation and di-carboxylation to prepare biomass derived polymer precursor. In Z-scheme Sv-ZnIn$_2$S$_4$/BiVO$_4$, spatially separating redox centers construction enhanced photogenerated holes and electrons separation was favorable for the benzyl radical generation and CO_2 carboxylation. Moreover, the introduction of S vacancies was helpful for the photoinduced electrons enrichment and substrate capture ability improvement.

1. Introduction

Excessive consumption of energy and overload emission of CO_2 have led to the increased environmental problems like greenhouse effect [1]. Therefore, the reutilization of waste carbon resource CO_2 has become an urgent goal for human beings. As an ideal carbon source in chemical synthesis, the conversion of CO_2 into valuable chemical compounds has received considerable attention in recent years owing to its abundance, easy availability and low toxicity [2,3]. At present, the conversion of CO_2 to CO, HCOOH or CH_4 etc. over heterogeneous photocatalytic materials has become a common and useful strategy for CO_2 reutilization [4–6]. Besides above CO_2 conversion to energy sources, the conversion of CO_2 into high value-added carboxylated products for pharmaceuticals and polymer industries has become a new hot carbon dioxide recycling research area since the photocatalytic continuous single-electron reduction of CO_2 was achieved in recent years [7]. For example, with Ni(bpy)$_3$Cl$_2$ sensitizer supported on α-Fe$_2$O$_3$ nanoparticles, Suman's group discovered an efficient photocatalyst for the carboxylation of 1,3-dicarbonyl compounds with CO_2, in which CO_2 was reduced to the CO_2 radical anion ($CO_2^{\bullet-}$) via direct single-electron

reduction [8]. At present, the CO_2 reutilization could be realized through the photocatalytic activation of C-halide bonds [9], aromatic ring sp C-H bonds [10] and unsaturated olefin sp^2 C-H bonds [11]. However, photocatalytic carboxylation of more inert bonds remains a great challenge. Aromatic alcohols widely exist in natural products, bioactive molecules and bulk chemicals [12], therefore, the achievement of the C-O bond activation and the CO_2 reuse to form corresponding high-value carboxylic acid products is an attractive and challenging task.

Renewable, easily available and abundant biomass and its platform products gradually become emerging energy alternatives to alleviate energy crisis [13–15]. As downstream products of lignin, furan biomass is recognized as one of the most important biomass derivatives [16]. Various catalytic technologies have been explored for the utilization of furan biomass. Sun's group used ZnIn$_2$S$_4$ nanosheets photocatalyst to achieve furfural or furfuryl alcohol C-C coupling reactions for the production of jet fuel precursors with above 90% high yield [17]. Besides the self-coupling of furan biomass, the furan carboxylation with CO_2 is also an attractive way to utilize furan biomass. However, considering the high energy barriers of CO_2 reduction [18], how to combine biomass

utilization and CO_2 recycling together remains a challenging issue for sustainable development. Yoshino's group found that furfural could be utilized to synthesis furan-2,5-dicarboxylic acid (FDCA) at 200 °C over molten salts promoted C-H activation along with CO_2 participated carboxylation [19]. Recently, our group utilized S-vacancies enriched $ZnIn_2S_4$ nanosheets photocatalyst to convert furfural to FDCA with up to 96% yield. FDCA was produced under mild conditions by means of the furfural in situ oxidation, furan ring sp^2 C-H activation and CO_2 photoreduction [20].

Metal sulfide/oxide photocatalysts have been widely utilized in hydrogen generation over water split [21–23], CO_2 reduction [24,25] and organic compounds synthesis [26] etc. For example, Yan's group reported that ultrathin CdS nanosheets could be used as photocatalyst for the amination of biomass-derived α-hydroxyl acids to produce amino acids in the presence of ammonia solution and visible light [27]. As one of the most studied metal sulfides, ternary metal sulfide $ZnIn_2S_4$ has narrow band gap and no toxic metal atoms [28,29]. Nevertheless, the drastic charge recombination of photoinduced carriers in pristine $ZnIn_2S_4$ limits its application in the field of photocatalysis. Various strategies, including morphology control [30], defect engineering [31] and Z-scheme heterojunction construction [32] etc., have been explored to promote the catalytic performance of $ZnIn_2S_4$. Yang's group demonstrated that the half unit cell $ZnIn_2S_4$ monolayer decorated with S vacancies exhibited excellent catalytic performance compared with the pristine $ZnIn_2S_4$ because of the photogenerated carrier lifetime increasement. The S vacancies enriched monolayer $ZnIn_2S_4$ could reach 13.478 mmol/g/h photocatalytic H_2 production rate with visible light [33]. Besides the defect engineering, Z-scheme heterojunction construction is also an attractive and popular way to improve the photocatalytic ability through the charge carriers recombination inhibition, the charge migration promotion as well as the stronger reduction and oxidation ability realization [34]. Xian's group integrated TiO_2 nanosheets in the $ZnIn_2S_4$ growth to prepare TiO_2-$ZnIn_2S_4$ direct Z-scheme, which showed enhanced photocatalytic water splitting activity and improved O_2 evolution efficiency. The TiO_2-$ZnIn_2S_4$ heterojunction maintained the highest redox potential and suppressed the photogenerated carries recombination [35]. As one of the most explored metal oxide photocatalysts, semiconductor $BiVO_4$, with characteristics of controllable morphology, strong solar light absorption ($\lambda < 550$ nm) and relatively narrow band gap (2.3–2.5 eV) [36], has attracted the widespread interest of scientists. $BiVO_4$ has exhibited excellent photocatalytic activities in hydrogen production, nitrogen fixation and CO_2 reduction because of its unique intrinsic properties [37].

In this work, Sv-$ZnIn_2S_4$/$BiVO_4$, with characteristics of spatially separating redox centers to improve the photogenerated carriers separation and controllable sulfur vacancies introduction to enhance the substrates capture ability, was constructed to explore the C-O activation of aromatic alcohols and the reutilization of waste carbon resource CO_2. Carbon chain increased aryl carboxylic acids could be prepared through aromatic alcohol esterification, photoinduced C-O activation and CO_2 carboxylation. It is worth noting that biomass derived asymmetric polymer precursor could also be prepared for the first time through furfuryl alcohol C-O activation and di-carboxylation with CO_2. This work sheds light on the possibility of integrating the utilization of CO_2 and biomass into the value-added chemicals preparation.

2. Experimental

2.1. Catalyst preparation

2.1.1. $ZnIn_2S_4$ (ZIS) preparation

68 mg $ZnCl_2$ and 293 mg $InCl_3\bullet4$ H_2O were dispersed in 25 mL H_2O and 5 mL glycol. After 30 min stirring, 150 mg thioacetamide (TAA) was added to the mixture. After another 30 min stirring, the solution was transferred to a 50 mL Teflon-lined autoclave and maintained at 120 °C for 12 h. After cooling, the product was obtained with centrifugation,

washed two times with ethanol and H_2O, and dried 6 h under vacuum for further use [38].

2.1.2. $BiVO_4$ preparation

Hydrothermal method was used to synthesize the decahedron $BiVO_4$. Typically, the precursors $Bi(NO_3)_3\cdot5$ H_2O (2.91 g) and NH_4VO_3 (0.7 g) were dispersed in the 2.0 M HNO_3 solution (50 mL). Subsequently, pH of above mixture was regulated to 2.0 by $NH_3\cdot H_2O$ accompany with the formation of orange precipitate. Above mixture was placed in 50 mL Teflon-lined autoclave for 2 h aging at room temperature and hydrothermal reaction at 200 °C for 24 h. A vivid yellow powder was obtained after hydrothermal reaction; product was washed thoroughly with ultrapure H_2O and EtOH, dried for 6 h under vacuum for further use [39].

2.1.3. ZIS/BVO and Sv-ZIS/BVO heterostructures preparation

Two-dimensional $ZnIn_2S_4$ nanosheets were decorated on the decahedron $BiVO_4$ surface over a low temperature solvothermal treatment. Generally, 20 mL of H_2O and 3 mL of glycerol were injected into a 50 mL flask; the pH was adjusted to 2.5 by HCl (0.5 M). Subsequently, $ZnCl_2$ (27.2 mg), $InCl_3\cdot4$ H_2O (58.6 mg) and TAA (30 mg) were added to the above mixture with 30 min stirring, then 52 mg of $BiVO_4$ produced above was introduced. The resulting mixture was stirred for 10 min and then solvothermal reaction was carried out at 80 °C for 2 h (Fig. 1). The brownish yellow product was washed 4 times with ultrapure water and EtOH, dried for 6 h in vacuum oven. For Sv-ZIS/BVO synthesis, the synthetic procedure was the same as ZIS/BVO except twice TAA (60 mg, 0.8 mmol) was added during the preparation.

2.2. Photocatalytic carboxylation

10 mg catalyst and 0.8 mmol K_2CO_3 were introduced to a 10 mL round bottom flask. 0.2 mmol benzyl alcohol, 1.05 equivalent of acetic anhydride (Ac_2O) and 3 mL N, N-Dimethylformamide (DMF) were injected into the flask under CO_2. After the reactor was heated at 50 °C for 5 h, photocatalytic reaction was carried out (0.75 W/cm^2 blue LED, 460 nm, 24 h). Photocatalyst was recycled with centrifugation for the reuse test. The supernatant was acidified with 2 mL 2 N HCl and then purified by column chromatography (CH_2Cl_2/MeOH/AcOH=3/1/ 0.1%), the obtained dried crude product was recrystallized with water and ethanol to give the pure desired product.

3. Result and discussion

3.1. Catalyst characterization

The X-ray diffraction (XRD) was measured to check the phase composition of $ZnIn_2S_4$, $BiVO_4$, ZIS/BVO and Sv-ZIS/BVO in Fig. 2. The peaks of $ZnIn_2S_4$ were in accordance with the hexagonal structure (JCPDS No. 65–2023) [40], and peaks at 20.4°, 27.3° and 47.0° were the (006), (102) and (110) facets of $ZnIn_2S_4$. $BiVO_4$ showed the feature peaks at 18.7°, 19.0°, 28.9°, 30.5°, 34.5°, 35.2°, 39.8°, 42.4°, 46.0°, 46.2°, 49.8°, 54.2°, 58.6°, 60.8°, which should be ascribed to the (110), (011), (121), (040), (200), (002), (211), (051), (241), (240), (202), (161), (321), (123) crystal planes [41]. The diffraction peaks of ZIS/BVO were almost the same as regular $BiVO_4$, which should be explained that the diffraction peaks of $ZnIn_2S_4$ were obviously smaller than $BiVO_4$ and the amount of $BiVO_4$ was more than $ZnIn_2S_4$ [42]. The absence of impurity peaks suggested the high purity and the maintained crystal phase of the original material. After S vacancies were constructed in ZIS/BVO, the phase composition of Sv-ZIS/BVO had no obvious change, which indicated that S vacancies had rather limited effect on the facets of ZIS/BVO. Moreover, the decreased intensity of $BiVO_4$ characteristic peaks in heterojunction ZIS/BVO indicated the successful combination between $BiVO_4$ and $ZnIn_2S_4$.

SEM image revealed that $BiVO_4$ had regular decahedron shape with diameter of 5–6 μm and relative smooth surface (Fig. 3a). The $ZnIn_2S_4$
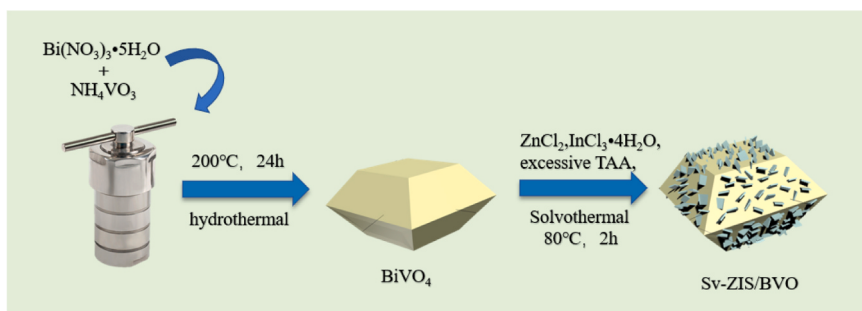
Fig. 1. Schematic diagram showing the synthesis of Sv-ZIS/BVO Z-scheme heterojunction.
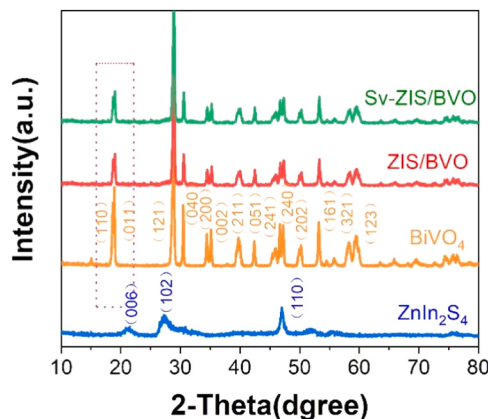

Fig. 2. Powder X-ray diffraction (XRD) patterns of ZIS, BiVO$_4$, ZIS/BVO and Sv-ZIS/BVO.

displayed microsphere architecture with 500–600 nm in size, which was consisted of 2D nanosheets (Fig. 3b). The SEM image of the ZIS/BVO heterostructure with the ZnIn$_2$S$_4$ on the BiVO$_4$ was presented in Fig. 3c, and the vertically grown ZnIn$_2$S$_4$ nanosheets were uniformly dispersed on the decahedral BiVO$_4$. After S vacancies were introduced to ZIS/BVO heterostructure, no obvious morphology change was observed in Sv-ZIS/BVO (Fig. 3d). TEM image in Fig. 3e also confirmed that the decahedron BiVO$_4$ was modified by ZnIn$_2$S$_4$ nanosheets. The high-resolution TEM image revealed that the apparent lattice fringes with interplanar spacing of 0.225 nm and 0.251 nm were in agreement with the (100) of the hexagonal ZnIn$_2$S$_4$ phase and the (002) of the monoclinic BiVO$_4$ phase (Fig. 3f). The TEM mapping (Fig. 3g) confirmed the presence of Bi, V, O, Zn, In, and S elements, which further demonstrated the successful construction of ZIS/BVO heterojunction.

X-ray photoelectron spectroscopy (XPS) was employed to check the chemical state and surface atomic composition of BiVO$_4$, ZnIn$_2$S$_4$, ZIS/BVO and Sv-ZIS/BVO. Fig. 4a showed the survey spectrum of all materials, which confirmed the existence of Bi, V, O, Zn, In, and S in Z-scheme heterojunction. Fig. 4b displayed the high resolution XPS of Bi 4 f, 164.2 and 158.9 eV were corresponding to Bi 4 $f_{5/2}$ and Bi 4 $f_{7/2}$ of Bi^{3+} species [43]. Furthermore, the S chemical states in Fig. 4b could be detected at 162.5 and 160.8 eV, which were S $2p_{1/2}$ and S $2p_{3/2}$. S vacancies, with feature of strong electron enrichment capability, could reduce the S atoms equilibrium electron cloud density along with the electrons transfer to S vacancies. Therefore, binding energy of S atoms was decreased accompany with S vacancies formation. For ZnIn$_2$S$_4$, two peaks at 452.3 and 444.8 eV were In $3d_{3/2}$ and In $3d_{5/2}$ (Fig. 4c). 1045.0 and 1022.1 eV were Zn $2p_{1/2}$ and Zn $2p_{3/2}$ (Fig. 4d) [44]. However, binding energies of Zn 2p and In 3d in ZIS/BVO exhibited some negative shift as compared with ZnIn$_2$S$_4$, which proved the successful fabrication of Z-scheme heterojunction. The slight negative shift of Zn 2p and In 3d in Sv-ZIS/BVO was detected after the introduction of S vacancies, which

suggested that S vacancies led to Zn and In coordination number reduce [45].

The optical properties of BiVO$_4$, ZnIn$_2$S$_4$, ZIS/BVO and Sv-ZIS/BVO were estimated by UV–vis diffuse reflectance spectra, which generally reflect the light absorption range and intensity of photocatalysts. The absorption edge of decahedron BiVO$_4$ and ZnIn$_2$S$_4$ were located at about 550 and 565 nm (Fig. 5a), which indicated that the catalysts could realize photocatalytic reaction through light response [46]. The Z-Scheme heterojunction ZIS/BVO hybrids displayed better visible light absorption, which confirmed that the introduction of ZnIn$_2$S$_4$ was good for the visible light response of BiVO$_4$ to some extent. As compared with ZIS/BVO, Sv-ZIS/BVO displayed light absorption improvement after the introduction of S vacancies, which should be owing to the defect energy level generation to improve the visible light absorption [47]. Meanwhile, band gaps of BiVO$_4$ and ZnIn$_2$S$_4$ were 2.41 and 2.24 eV (Fig. 5b). To identify the conduction band (CB) potential and semiconductor type of BiVO$_4$ and ZnIn$_2$S$_4$, Mott–Schottky (M–S) curves were carried out. In Figs. 5c and 5d, BiVO$_4$ and ZnIn$_2$S$_4$ showed the n-type feature as the positive slope of the M-S curves, and the flat band potentials were 0.21 and − 0.99 V (vs Ag/AgCl, pH = 7) in line with the intercept of the tangent of M-S curves. Fermi level is almost equal to flat band potential for n-type semiconductor, and flat band potential is close to the CB potential [48]. CB potentials of BiVO$_4$ and ZnIn$_2$S$_4$ were calculated as 0.01 and − 1.19 V (vs NHE). In combination with Fig. 4b, the valence bands (VB) of BiVO$_4$ and ZnIn$_2$S$_4$ should be 2.40 and 1.05 V. In combination with the Mott-Schottky formula [49], it can be seen that the carrier concentration is inversely proportional to the slope of the curve, and the lower the slope, the greater the carrier concentration in the semiconductor. The Mott-Schottky slopes of ZIS and BiVO$_4$ (Fig. S2) displayed that the slope of ZIS was smaller than that of BiVO$_4$, thus, the carrier concentration of ZIS was higher than that of BiVO$_4$. When heterojunction was formed with ZIS and BiVO$_4$, charge carriers would have the tendency of diffusing from charge carriers enriched ZIS to charge carriers deficient BiVO$_4$, therefore, an internal electric field would be formed.

The photocurrent response was exhibited in Fig. 6a, photocurrent-time experiment was conducted with several light on/off cycles. All photocatalysts had light response under light irradiation; photocurrent density of photocatalysts rapidly increased and remained stable after light was turned on, which indicated that catalysts were rather sensitive to light. The current density was Sv-ZIS/BVO > ZIS/BVO > ZIS > BiVO$_4$. Moreover, there had spikes in ZIS/BVO and Sv-ZIS/BVO while light was on, which should be ascribed to the transient accumulation of photoinduced charges, indicating the generation of massive valid carriers in ZIS/BVO and Sv-ZIS/BVO instead of recombination [50]. The linear scanning voltage (LSV) curve of ZIS, BiVO$_4$, ZIS/BVO and Sv-ZIS/BVO was tested to clarify the existence of internal electric field in ZIS/BVO and Sv-ZIS/BVO in Fig. 6b [51]. The photocurrent densities of ZIS/BVO and Sv-ZIS/BVO were 1.1 uA/cm^2 and 1.6 uA/cm^2 (vs. RHE), while the current densities of ZIS and BiVO$_4$ were 0.58 uA/cm^2 and 0.3 uA/cm^2. All of the LSV result was corresponded to photocurrent response in Fig. 6a. The obviously increased photocurrent density
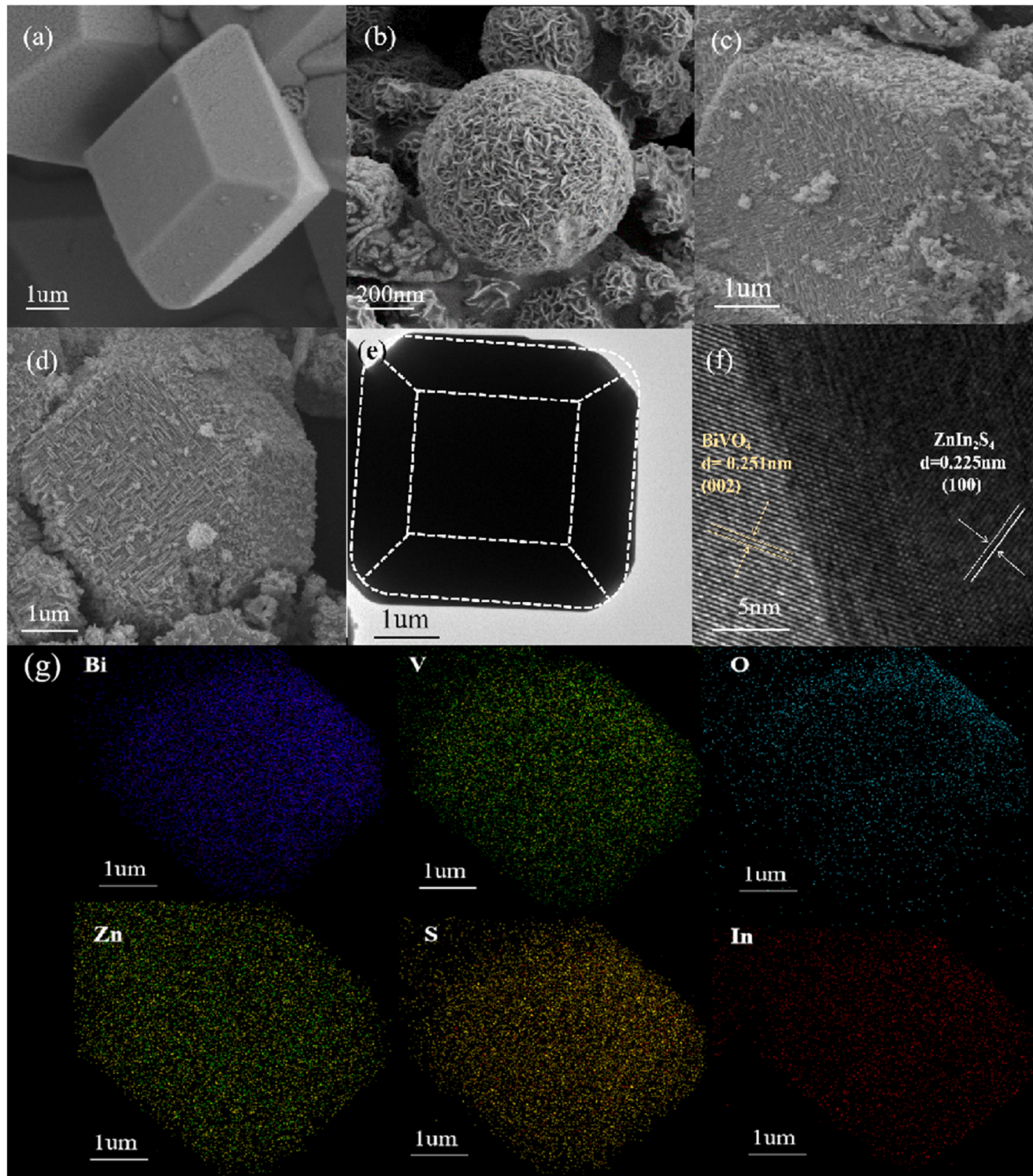
Fig. 3. SEM images of a) BiVO$_4$, b) ZnIn$_2$S$_4$ nanoflowers, c) ZIS/BVO heterojunction and d) Sv-ZIS/BVO heterojunction. e) TEM image and f) HRTEM of Sv-ZIS/BVO heterojunction. g) Element mapping images of Sv-ZIS/BVO.

indicated the existence of internal electric field in heterojunction ZIS/BVO and Sv-ZIS/BVO, therefore, the migration of photogenerated carriers was boosted. After the S vacancies were introduced, the further increased photocurrent density in Sv-ZIS/BVO demonstrated that electron capture capability of S vacancies improved the photocarriers separation [52]. Moreover, ultraviolet photoelectron spectroscopy (UPS) was carried out to measure the ionization potential (equal to the E$_{VB}$)

and work function (φ) of BiVO$_4$ and ZnIn$_2$S$_4$. As illustrated in Fig. 7, the cutoff energies (E$_{cutoff}$) of BiVO$_4$ and ZnIn$_2$S$_4$ were 16.61 and 16.78 eV, and their corresponding onset energies (E$_{onset}$) were 2.53 and 2.03 eV. The E$_{VB}$ of BiVO$_4$ and ZnIn$_2$S$_4$ were 7.14 and 6.47 eV by subtracting the width of the He I UPS from the excitation energy (21.22 eV): E$_{VB}$ = 21.22 − (E$_{cutoff}$ − E$_{onset}$). The two energies were calculated to be 2.7 and 2.03 V according to the reference standard (0 V versus reversible
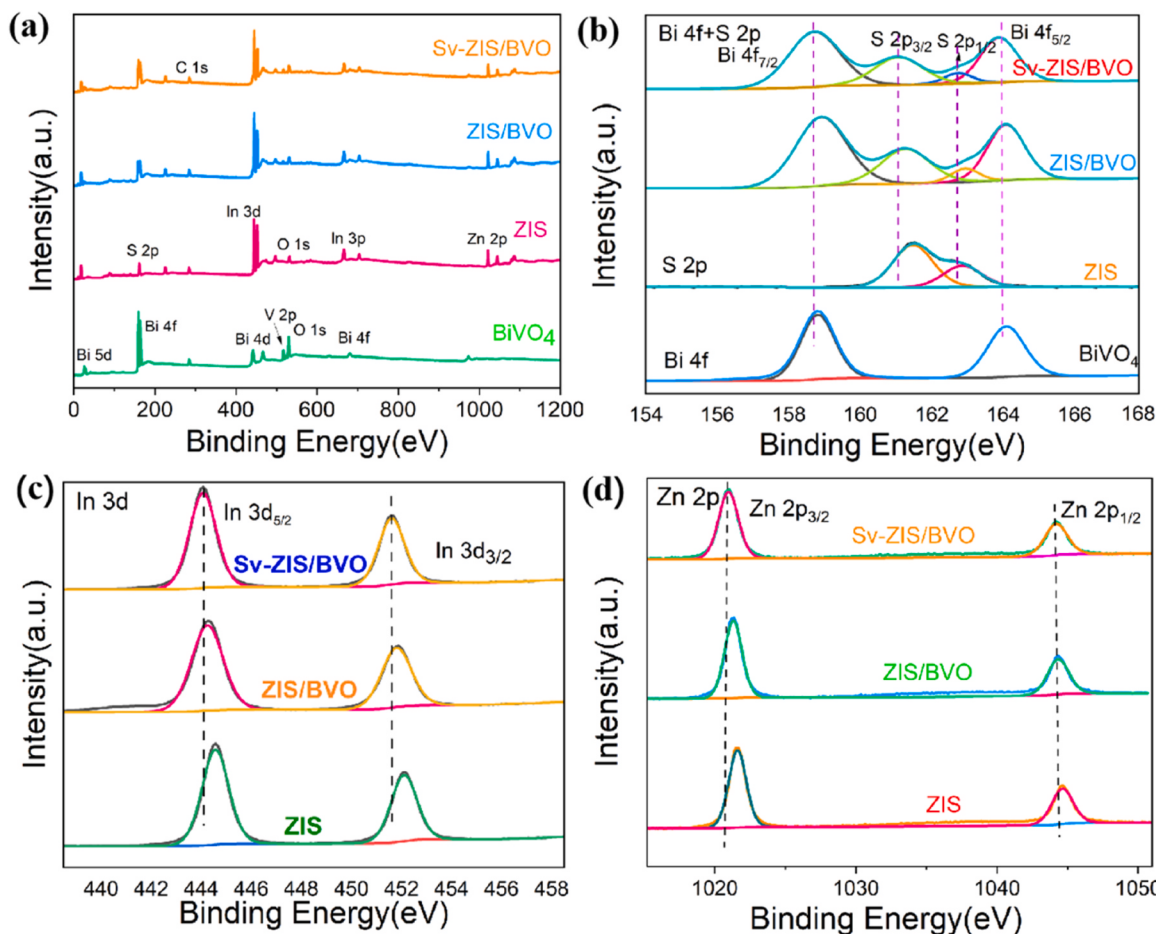
Fig. 4. (a) XPS survey, (b) Bi 4 f and S 2p, (c) In 3d, (d) Zn 2p for ZIS, $BiVO_4$, ZIS/BVO and Sv-ZIS/BVO.

hydrogen electrode equals -4.44 eV). The E_{VB} was similar to above calculated VB potentials. In addition, the φ of $BiVO_4$ and $ZnIn_2S_4$ were obtained to be 4.61 and 4.44 eV ($\varphi = 21.22 - E_{cutoff}$). Based on above result, $e^- - h^+$ pairs of $BiVO_4$ and $ZnIn_2S_4$ could be separated with light irradiation; e^- could be excited to the CB and h^+ was remained in VB. The Fermi level (E_F) is approximately equal to flat band potential of n-type semiconductor, and the E_F of $BiVO_4$ and $ZnIn_2S_4$ was about 0.21 eV and -0.99 eV (vs Ag/AgCl, pH = 7). Therefore, $BiVO_4$ showed a larger φ (4.61 eV) and a lower Fermi level before contact, while $ZnIn_2S_4$ exhibited a smaller φ (4.44 eV) and a higher Fermi level. Once the heterojunction was formed, their Fermi energy levels immediately reach equilibrium, facilitating the formation of an internal electric field.

Electrochemical impedance spectroscopy (EIS) of Sv-ZIS/BVO, ZIS/BVO, ZIS and $BiVO_4$ were tested to determine the electrical conductivity (Fig. 6c). In comparison with ZIS and $BiVO_4$, Z-scheme heterojunction ZIS/BVO showed a decreased semicircle arc diameter, which suggested that the photogenerated electrons in ZIS/BVO experienced less resistance. After S vacancies introduction, Sv-ZIS/BVO had smaller arc diameter than ZIS/BVO, which was in agreement with the photocurrent density result. Above result demonstrated that the ZIS/BVO heterojunction formation and the S vacancies introduction were beneficial to improve the use of photogenerated e^- and h^+ for the catalytic activity enhancement [53]. Electron paramagnetic resonance (EPR) was carried out to testify the S vacancies in Fig. 6d, no EPR signal was observed in ZIS/BVO. After excessive TAA was added, the strong EPR signal at 2.007 in Sv-ZIS/BVO should be explained that excessive TAA would adsorb and cluster on the $ZnIn_2S_4$ nanocrystals surface to inhibit the crystal growth, leading to the formation of sulfur vacancies [54].

DMPO-ESR spin-trap experiment was applied to demonstrate the appropriateness of the Z-scheme characteristics, and to analyze the location of e^- and h^+. DMPO was used as the radical capture reagent for superoxide radical ($\bullet O_2^-$) and hydroxyl radical ($\bullet OH$). In Figs. 8b-8c, almost no feature peak of DMPO-$\bullet O_2^-$ was detected over $BiVO_4$ after 3 min illumination, which should be explained that the CB of $BiVO_4$ is higher than $O_2/\bullet O_2^-$ (-0.33 V vs NHE) [55]. Meanwhile, the $\bullet O_2^-$ was observed over $ZnIn_2S_4$ on account of the appropriate CB potential (-1.19 V vs NHE). To our delight, stronger DMPO-$\bullet O_2^-$ peaks were observed over ZIS/BVO with light, which indicated that photoinduced electrons were accumulated on the CB of $ZnIn_2S_4$ rather than $BiVO_4$. $\bullet OH$ could be generated through the oxidation of photogenerated holes on the VB of $BiVO_4$ (2.40 V vs NHE). As the VB level of $ZnIn_2S_4$ (1.05 V vs NHE) was lower than $\bullet OH/OH^-$ (1.99 V vs NHE) and $H_2O/\bullet OH$ (2.37 V vs NHE), $\bullet OH$ could not be generated with $ZnIn_2S_4$ through the reduction on CB [56]. Similarly, stronger peaks of DMPO-$\bullet OH$ were observed with ZIS/BVO, which was deduced that the photoinduced holes generally remained on higher potential VB of $BiVO_4$. With the Sv-ZIS/BVO catalyst, further enhanced DMPO-$\bullet O_2^-$ and DMPO-$\bullet OH$ signals were detected, which should be explained that the electron capture capacity of the S-vacancies increased the carrier separation efficiency for the redox capacity further enhancement. Above results were in consistent with the proposed Z-scheme mechanism (Fig. 8a).

3.2. Photocatalytic carboxylation reaction

Aromatic alcohols are recognized as environmental friendly substrate because of the low toxicity, stability and easy availability. The achievement of the C-O bond activation and the CO_2 reuse to form corresponding high-value carbon chain increased carboxylic acid
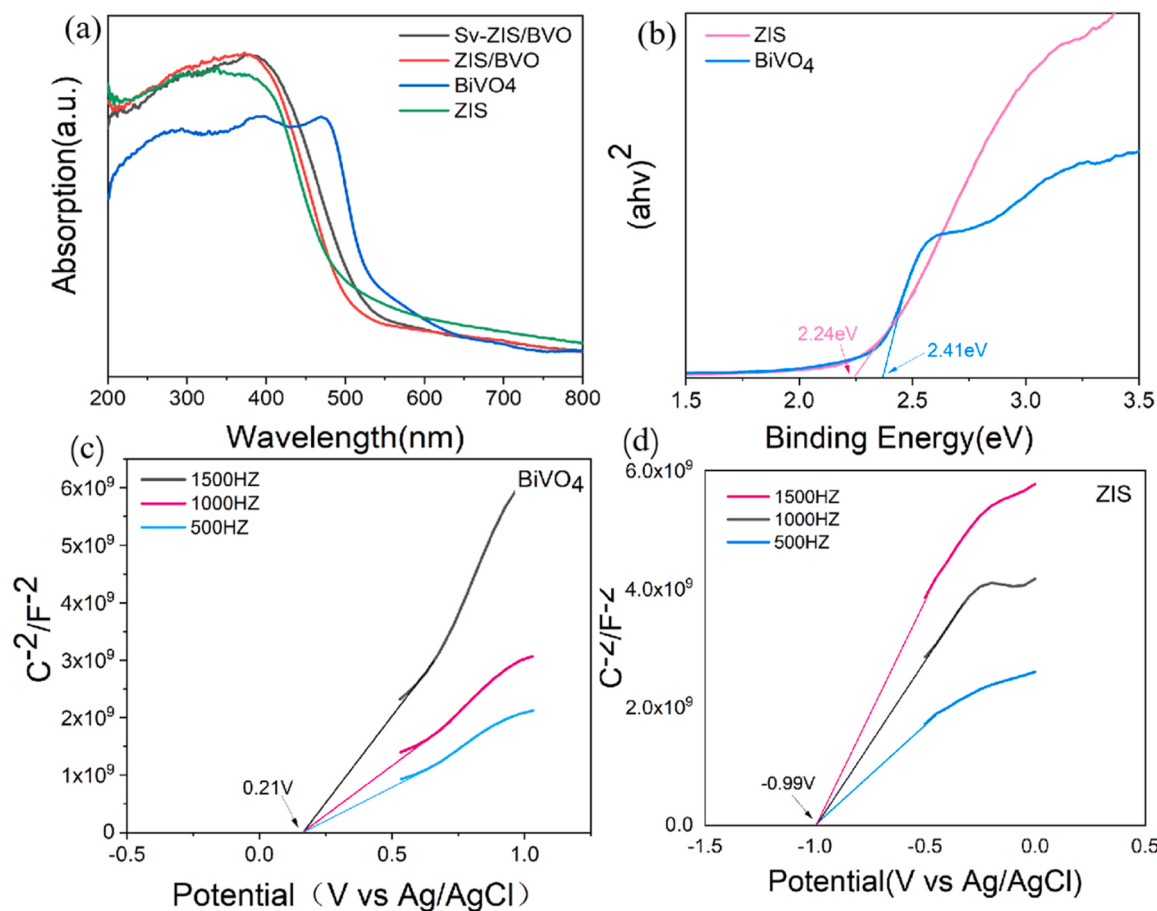
Fig. 5. (a) UV–vis absorption spectrum of ZIS, $BiVO_4$, ZIS/BVO and Sv-ZIS/BVO; (b) band gaps of ZIS and $BiVO_4$. Mott-Schottky (M-S) plots of (c) $BiVO_4$ and (d) ZIS.

products is a rather attractive and challenging task. Till now, there still has no relevant report in the field of heterogeneous photocatalytic aromatic alcohols carboxylation with CO_2 to produce carbon chain increased carboxylic acid product. Benzyl alcohol carboxylation with CO_2 was chosen as the model reaction to explore the possibility of aryl alcohol substrates carboxylation with CO_2 to prepare value-added acids. The designed phenylacetic acid catalytic synthesis route includes acetic anhydride acylation of benzyl alcohol, C-O bond cleavage of acylation product and CO_2 carboxylation. $ZnIn_2S_4$ and its composites were utilized to explore the photocatalytic carboxylation reaction, and the result was shown in Table 1.

100% benzyl alcohol conversion with 37% chemoselectivity to phenylacetic acid was achieved with flower shape $ZnIn_2S_4$ microspheres under $0.15w/cm^2$ blue led light irradiation (Table 1, entry 1). The carboxylation reaction was also examined under different light wavelengths (Table S1) and it was found that 460 nm was the most suitable light wavelength for the carboxylation reaction. To elucidate whether CO_2 was the only C source in the carboxylation, N_2 was utilized instead of CO_2, only acylation product **1d** was detected (Table 1, entry 2). Without light or photocatalyst, just acylation product **1d** demonstrated that light and photocatalyst were the critical factor of the photoctalytic carboxlytion reaction (Table 1, entries 3–4). In theory, benzyl alcohol-CO_2 intermediate in-situ formation might be one simple route for carbon chain increased carboxylation product **1d** preparation. We conducted the carboxylatic reaction in the absence of acetic anhydride to verify the possibility of benzyl alcohol-CO_2 intermediate in-situ formation in this system. However, just benzoic acid was detected with 100% benzyl alcohol conversion (Table 1, entry 6), which might be explained that benzyl alcohol was completely oxidized to benzoic acid due to the strong oxidation ability of the photocatalyst without acylation protective

group. $0.75 W/cm^2$ led light was used to promote the photocatalytic carboxylation, and 62% chemoselectivity to phenylacetic acid was achieved (Table 1, entry 7). Trimethylacetic anhydride and trifluoroacetic anhydride were also utilized to replace acetic anhydride (Table 1, entries 8–9), the reduced chemoselectivity to phenylacetic acid indicated that acetic anhydride was the most suitable acylation reagent for this catalytic carboxylation. Different base additive like K_3PO_4, Na_2CO_3 were used to explore the impact of base on the carboxylation reaction, and similar photocatalytic performance was obtained (Table 1, entries 10–11). We also tested the photocatalytic carboxylation reaction with other solvent like acetonitrile and methanol (Table 1, entries 12–13), the result showed that DMF was the best solvent to produce phenylacetic acid. We further employed $BiVO_4$, ZIS/BVO and Sv-ZIS/BVO to explore the influence of the materials characteristic on photocatalytic carboxylation. 32% chemoselectivity to phenylacetic acid was obtained over $BiVO_4$ (Table 1, entry 14). With Z-scheme ZIS/BVO, the up to 79% chemoselectivity to phenylacetic acid should be explained that the construction of spatially separated redox center in Z-scheme ZIS/BVO improved the separation and redox capacity of photocarriers, the intimate contact of heterojunction interface enhanced the migration of photocarriers and the presence of internal electric field accelerated the Z-scheme path route migration of photogenerated electrons (Table 1, entry 15). After the S vacancies introduction, the 98% yield of phenylacetic acid was obtained with Sv-ZIS/BVO (Table 1, entry 16), which was interpreted that S vacancies would ameliorate the CO_2 adsorption, photogenerated electrons capture as well as CO_2 photoreduction. In short, Z-scheme photocatalyst Sv-ZIS/BVO based redox ability improvement, photocarriers separation promotion and substrate adsorption enhancement were important factors in the effective acylation product C-O bond activation and CO_2 carboxylation to prepare
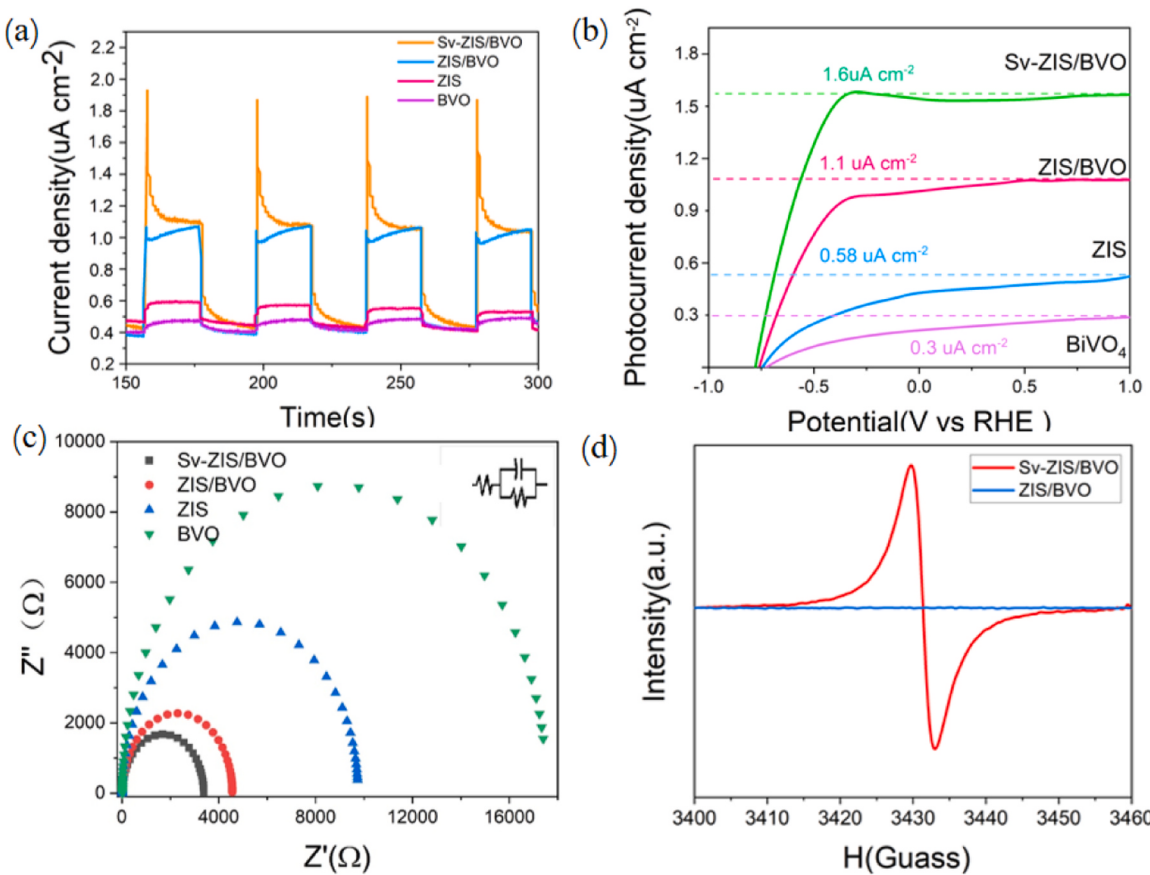
Fig. 6. (a) photocurrent response, (b) LSV plots, (c) electrochemical impedance spectroscopy (EIS) of the as-prepared samples, (d) EPR spectra of ZIS/BVO and Sv-ZIS/BVO.
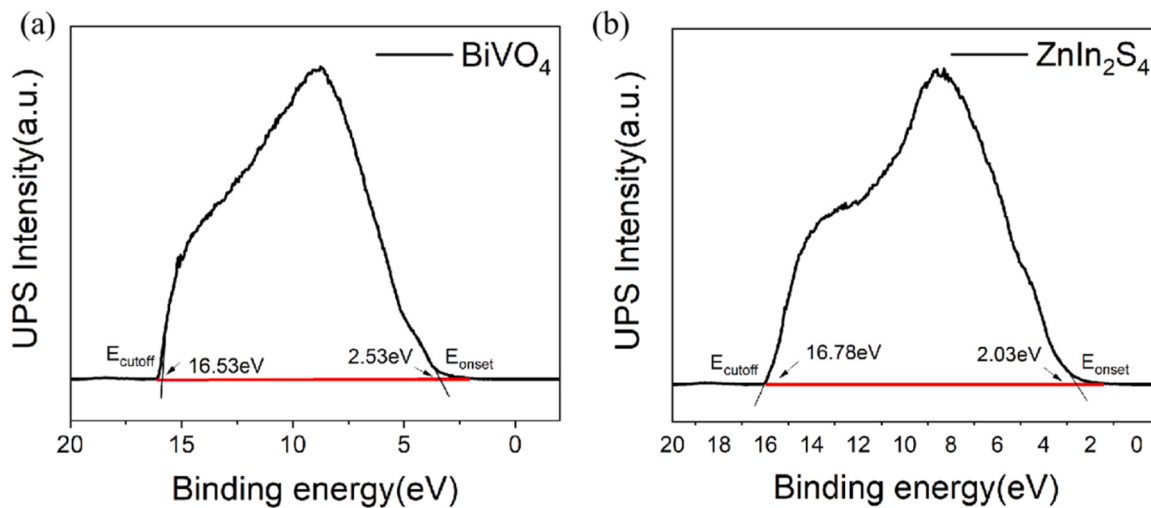

Fig. 7. UPS analysis of (a) $BiVO_4$ and (b) $ZnIn_2S_4$.

phenylacetic acid.

Various aromatic acids would serve as synthetic precursors for many biologically active molecules because the carboxyl group could be easily derived as pharmacologically important amine, lactam and lactone units. The carbon chain increased carboxylation of other aromatic alcohols with CO_2 was carried out under the optimized conditions to clarify the practicality of photocatalyst Sv-ZIS/BVO in Table 2. In order to explore the tolerability of substituted groups in aromatic alcohols, methyl and methoxy groups were chosen as electron donating groups

(Table 2, entries 2–3). 47% *p*-methoxyphenyl acetic acid and 51% *p*-methyl phenylacetic acid were produced from *p*-methoxy benzyl alcohol and *p*-methyl benzyl alcohol under the optimized conditions. Electron-donating effect in aromatic alcohols had an adverse effect on this photocatalytic carboxylation process, which might be explained that electron-donating groups were unfavorable for the generation of benzyl radical. Trifluoromethyl and nitro were chosen as electron-withdrawing groups in this catalytic carboxylation system (Table 2, entries 4–7). As compared with electron-donating groups, the electron-withdrawing
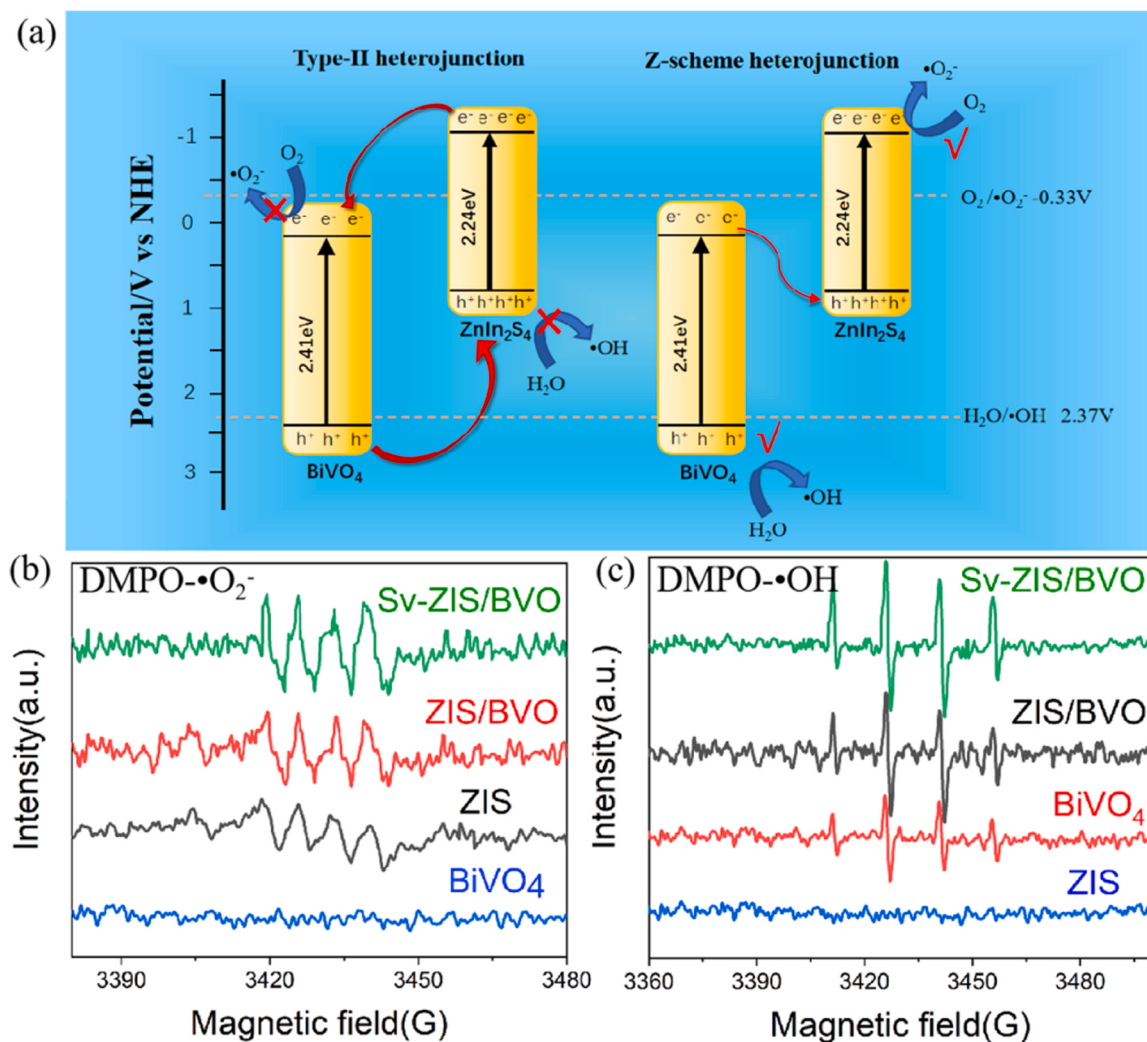
Fig. 8. (a) Schematic representation of Z-scheme electron-hole transfer mechanism, DMPO spin-trapping ESR spectra recorded for •O$_2^-$ (b), and •OH (c) with ZnIn$_2$S$_4$, BiVO$_4$, ZIS/BVO and Sv-ZIS/BVO.

groups substituted aromatic alcohols showed relatively higher photocatalytic activity (Table 2, entries 2–3 vs 4–7). In addition, *o*-, *m*- and *p*-substituted trifluoromethylphenylethanols were employed to investigate the influence of steric hindrance on the carboxylation reaction (Table 2, entries 5–7). The similar yield of carbon chain increased acids indicated that steric effect had no obvious influence on aromatic alcohols carboxylation with CO$_2$ under the optimized conditions. The efficient utilization of biomass and its derivatives is the core issue of sustainable development. As an important biomass derived product accompany with the degradation of lignin, vanillyl alcohol is commonly used to produce renewable epoxy thermosetting resins [57]. Here, vanillyl alcohol was employed to produce carbon chain increased and value-added homovanillic acid under the optimized carboxylation conditions with the advantages of simplicity, high efficiency and environmental pollution avoidance. 72% yield of homovanillic acid 9b has been produced over heterojunction photocatalyst Sv-ZIS/BVO (Table 2, entry 8). Dicarboxylated products, which are traditionally synthesized under harsh conditions like strong oxidants utilization and high temperature, have been widely used as polymer precursors, pharmaceutical intermediates, and cosmetics [58]. Photocatalytic dicarboxylation strategy would be a rather efficient and green method for the carbon dioxide reutilization. So far, there has no CO$_2$ dicarboxylation report in heterogeneous catalytic systems. 2-thiophene methanol was used to test the practicability of dicarboxylation (Table 2, entry 9), 86% yield of

asymmetric carboxylic acid **9b** could be prepared from 2-thiophene methanol with the consumption of 2 equivalents CO$_2$ under relatively mild catalytic reaction conditions.

The above success of biomass alcohol carboxylation (Table 2, entry 8) and heterocyclic compound dicarboxylation (Table 2, entry 9) prompted us to deepen the practical application of Sv-ZIS/BVO catalytic system. In our previous work, S vacancies enriched ZnIn$_2$S$_4$ nanosheets was utilized to prepared high value furan-2,5-dicarboxylic acid (FDCA), which could be utilized as biomass-derived degradable polymer precursor [20]. To further enrich the structural variation of biomass derived degradable polymer precursors, we try to challenge asymmetric dicarboxylation acid polymer precursor production from furfuryl alcohol, which could be easily obtained from natural environment. The ^{1}H NMR and ^{13}C NMR spectra in Fig. 9 demonstrated that 5-carboxymethylfuran-2-carboxylic acid could be successfully synthesized from furfuryl alcohol and two equivalents CO$_2$ with the isolated yield up to 95% over Z-scheme heterojuction photocatalyst Sv-ZIS/BVO. The 5 position of furan ring in furfuryl alcohol is active (C-H pKa ~35) [59,60], thus, not only the C-O bond could be fractured to prepare carbon chain increased aryl carboxylic acid, the C-H bond at 5 position of furan ring could also be activated by photogenerated holes to generate free radical, which could react with CO$_2$ to form biomass derived asymmetric dicarboxylic acid. Such biomass-derived asymmetric carboxylic acid could not just be used as degradable polymer precursor from the environmental

Table 1
Result for optimization of photocatalytic carboxylation reaction parameters.[a].

Entry	Catalyst	Base	Solvent	Acylation reagents	Conversion (%)[b]	Selectivity (%) 1b	1d
1	ZIS	K_2CO_3	DMF	Ac_2O	100%	37%	63%
2[c]	ZIS	K_2CO_3	DMF	Ac_2O	100%	-[d]	100%
3[e]	ZIS	K_2CO_3	DMF	Ac_2O	100%	-	100%
4	-	K_2CO_3	DMF	Ac_2O	100%	-	100%
5	ZIS	-	DMF	Ac_2O	68%	-	100%
6	ZIS	K_2CO_3	DMF	-	100%[f]	-	-
7[g]	ZIS	K_2CO_3	DMF	Ac_2O	100%	62%	38%
8[g]	ZIS	K_2CO_3	DMF	Piv_2O	76%	46%	54%
9[g]	ZIS	K_2CO_3	DMF	TFAH	100%	39%	61%
10[g]	ZIS	K_3PO_4	DMF	Ac_2O	100%	55%	45%
11[g]	ZIS	Na_2CO_3	DMF	Ac_2O	100%	58%	42%
12[g]	ZIS	K_2CO_3	MECN	Ac_2O	87%	17%	83%
13[g]	ZIS	K_2CO_3	CH_3OH	Ac_2O	67%	44%	56%
14[g]	BiVO4	K_2CO_3	DMF	Ac_2O	100%	32%	68%
15[g]	ZIS/BVO	K_2CO_3	DMF	Ac_2O	100%	79%	21%
16[g]	Sv-ZIS/BVO	K_2CO_3	DMF	Ac_2O	100%	98%	2%

a Reaction conditions: photocatalyst (10 mg), benzyl alcohol (0.2 mmol), base (0.8 mmol) and solvent (2 mL), benzyl alcohol was firstly acylated with Ac_2O at 50 °C, and then irradiated with 0.15 Wcm^{-2} blue LED ($\lambda = 460$ nm) for 24 h with 1 atm CO_2 at room temperature. ZIS: $ZnIn_2S_4$, ZIS/BVO: $ZnIn_2S_4/BiVO_4$ heterojunction, Sv-ZIS/BVO: S vacancies enriched $ZnIn_2S_4/BiVO_4$ heterojunction, TFAH: trifluoroacetic anhydride.
[b] Yields and selectivities were determined by HPLC.
[c] The atmosphere was N_2.
d No conversion detected.
[e] No visible light.
[f] The product was benzoic acid.
[g] 0.75Wcm^{-2} blue LED ($\lambda = 460$ nm) instead.

perspective, but provide the diversity for the biodegradable polymer application performance adjustment. As a contrast, traditional 5-carbox-ymethylfuran-2-carboxylic acid preparation required complicated steps, harsh reaction conditions and high costs, therefore, the synthetic route here is green and attractive because biomass platform reactant furfuryl alcohol could consume 2 equivalents CO_2 under relatively mild conditions.

3.3. Photocatalytic carboxylation mechanism

In order to further determine the reaction process, kinetic experiment was conducted (Fig. 10a). Only acylation product benzyl acetate was detected in the initial 5 h esterification process under mild conditions. Benzyl alcohol was completely transformed to benzyl acetate intermediate in the absence of light after 5 h. Benzyl alcohol or benzyl acetate intermediate could not react with carbon dioxide under no light, which indicated that photocatalysis played an important role in the generation of benzyl radical and the reduction of carbon dioxide. The benzyl acetate decreased under light irradiation accompany with the detection of phenylacetic acid. The yield of phenylacetic acid gradually increased in the following 24 h, and 98% yield of phenylacetic acid could be achieved as a single product after the reaction. No other by-products were detected in the photocatalytic process, which not only indicated the moderate redox capacity with Z-scheme Sv-ZIS/BVO material, but also demonstrated the matched efficiency between generation of benzyl radicals and photocatalytic reduction of carbon dioxide over redox centers spatially separated Sv-ZIS/BVO. The reuse of photo-catalyst Sv-ZIS/BVO was carried out after the reaction. Sv-ZIS/BVO was recovered through centrifugation and utilized for subsequent carboxyl-ation process. Recovered Sv-ZIS/BVO was reutilized for 4 times with maintained catalytic performance (Fig. 10b). In addition, no obvious change in the XRD was observed in recycled catalyst, illustrating the stability of Sv-ZIS/BVO (Fig. S1).

To study the mechanism of photocatalytic benzyl alcohol C-O activation along with carboxylation with CO_2, different control experiments were carried out in Scheme 1. The radical scavenger TEMPO (6 equiv.) was introduced to the catalytic carboxylation (Scheme 1a) to check whether benzyl free radicals were generated during the benzyl alcohol C-O activation. Carboxylation reaction was completely suppressed and 19% capture product 1c was detected (the LC-MS of 1c was provided in the supporting information), which demonstrated the generation of benzyl radical intermediates. KI (4 equiv.) was utilized as hole trapping agent to exam the participation of photogenerated holes in carboxyla-tion. No phenylacetic acid was produced while KI was added (Scheme 1b), which suggested that holes were participated in benzyl alcohol C-O activation to form benzyl free radicals. When electron scavenger $K_2S_2O_8$ (4 equiv.) was added to the photocatalytic system (Scheme 1c) [61], no phenylacetic acid formation indicated that photogenerated electrons participated the carboxylation, therefore, the photogenerated electrons should be transferred to benzyl free radicals to form benzyl radical anion, which could nucleophilic attack CO_2 to produce carbon chain increased acid [62]. Moreover, carbonate detection experiment was carried out to clarify whether the benzyl alcohol-CO_2 intermediate in-situ formation would be one possible route for carbon chain increased carboxylation product preparation (Scheme 1d). Potassium tert-butyl alcohol was utilized to realize the direct reaction between benzyl alcohol and CO_2 [63], and carbonic ester 1e was obtained after the esterification with MeI. 1e could also experience a photoredox catalyzed carboxylation to give the desired 1b with 83% yield. Carbonate detec-tion experiment in Scheme 1d suggested that benzyl alcohol-CO_2 in-termediate in-situ formation could theoretically realize the 1b preparation, however, the reality was that just benzoic acid was detec-ted without Ac_2O (Table 1, entry 6). Difference between theory and reality might be explained that strong oxidation capacity of the photo-catalyst Sv-ZIS/BVO was more inclined to accelerate benzyl alcohol oxidation for benzoic acid production rather than promote the benzyl

Table 2

Substrates scope of photocatalytic carboxylation with CO_2.

Entry	Substrate	Product	Conversion (%)[a]	Yield (%)[b]
1	1a	1b	100%	98%
2	2a	2b	100%	47%
3	3a	3b	100%	51%
4	4a	4b	100%	62%
5	5a	5b	100%	85%
6	6a	6b	100%	82%
7	7a	7b	100%	87%
8	8a	8b	100%	72%
9	9a	9b	100%	86%
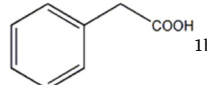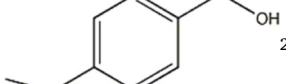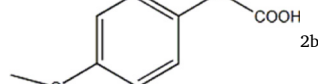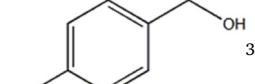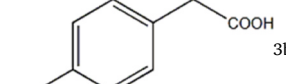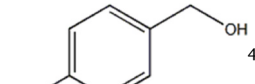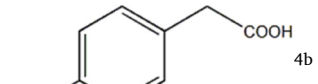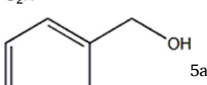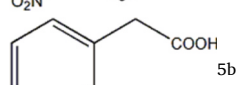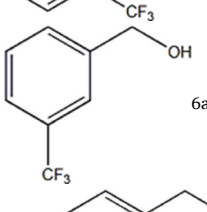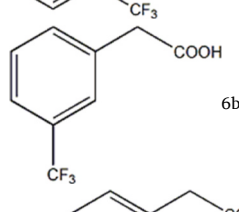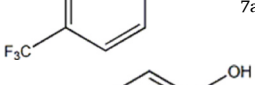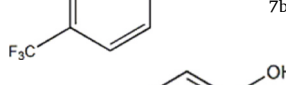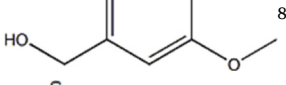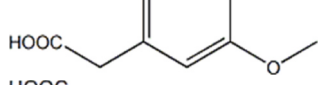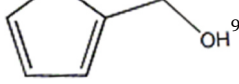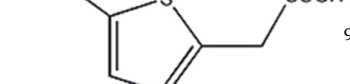
Note: The reaction conditions were the same as in Table 1, entry 16.

[a] Substrate conversion to carboxylated product was determined by HPLC.

[b] Isolated yield.

alcohol-CO_2 intermediate in-situ formation for carboxylation realization. As the acetate ion would be generated during the esterification and the benzyl radicals formation process, it is necessary to clarify the state of the acetate ion in the reaction process. The ion chromatography was utilized to monitor the acetate ion, and the result showed that acetate ion was gradually consumed during the photocatalytic carboxylation reaction. Some oxidized species may be generated accompany with the acetate ion consumption. Considering the fact that no carboxylated product was detected when N_2 was utilized instead of CO_2 (Table 1, entry 2), it should be explained that most oxidized species of acetate ion probably could not participate in carboxylation. Even though a small amount of CO_2 might be generated during the acetate ion consumption, the CO_2 concentration was too low to trigger carboxylation reaction.

Based on the control experiments, reaction mechanism was suggested in Scheme 2. The benzyl alcohol converted to intermediate **1d** with Ac_2O and K_2CO_3. The holes and electrons were generated in photocatalyst Sv-ZIS/BVO with light, the photogenerated electrons produced in VB of $BiVO_4$ would transfer to CB of $ZnIn_2S_4$. The intermediate **1d** undergone C(sp^3)-O bond cleavage with the synergistic effect of holes

and K_2CO_3 to generated benzyl radical accompany with carboxylate radical cation release, which would be subsequently degraded into oxidized species. Because of the Z-scheme characteristic of photocatalyst, the photogenerated electrons would transfer to the photocatalyst surface rapidly and then be captured by S vacancies. The photogenerated electron could attach to a benzyl radical to generate benzylic radical **B**, and then the photogenerated electron reduction of benzylic radical **B** could form the benzylic carbanion **C**, which would experience nucleophilic attack with CO_2 to produce carboxylate [64], then phenylacetic acid was obtained after simple acidification.

4. Conclusion

In conclusion, S vacancies enriched Z-scheme Sv-$ZnIn_2S_4$/$BiVO_4$ was designed for aromatic alcohols carboxylation with 1 atm CO_2 under light irradiation. Carbon chain increased carboxylic acid could be easily produced through acetic anhydride assisted esterification, photogenerated holes oxidization induced benzyl radical generation and subsequent CO_2 carboxylation. In particular, high value-added
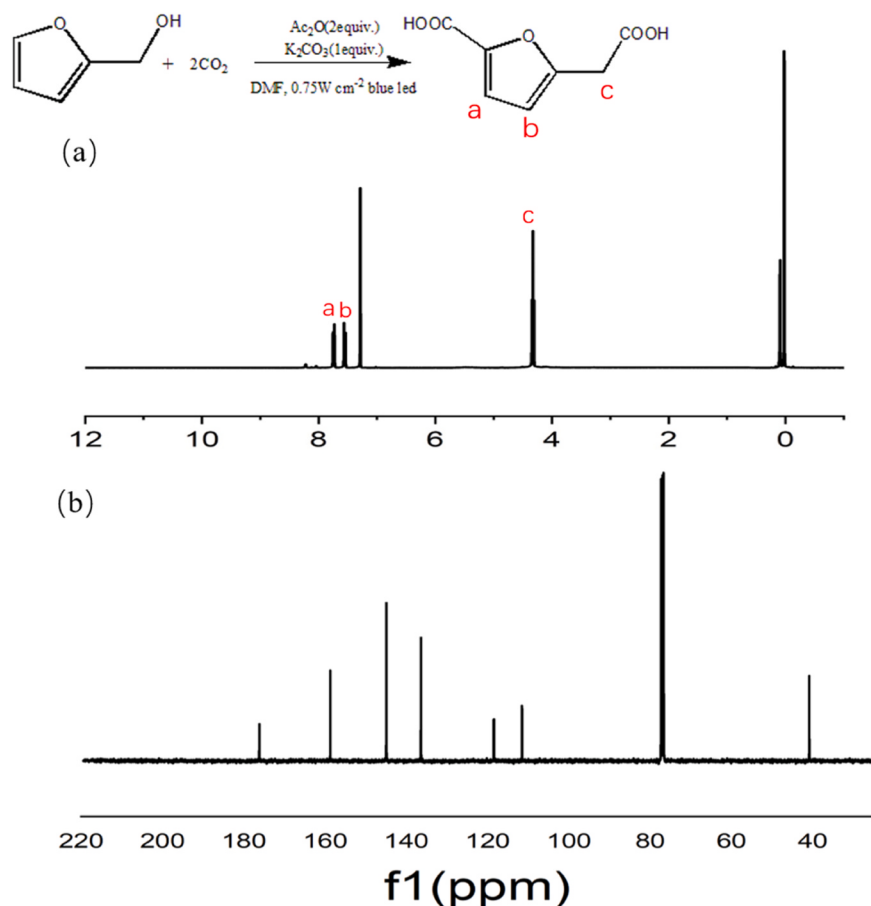
Fig. 9. (a) ^{1}H NMR spectra and (b) ^{13}C NMR of photocatalytic furfuryl alcohol carboxylation product.
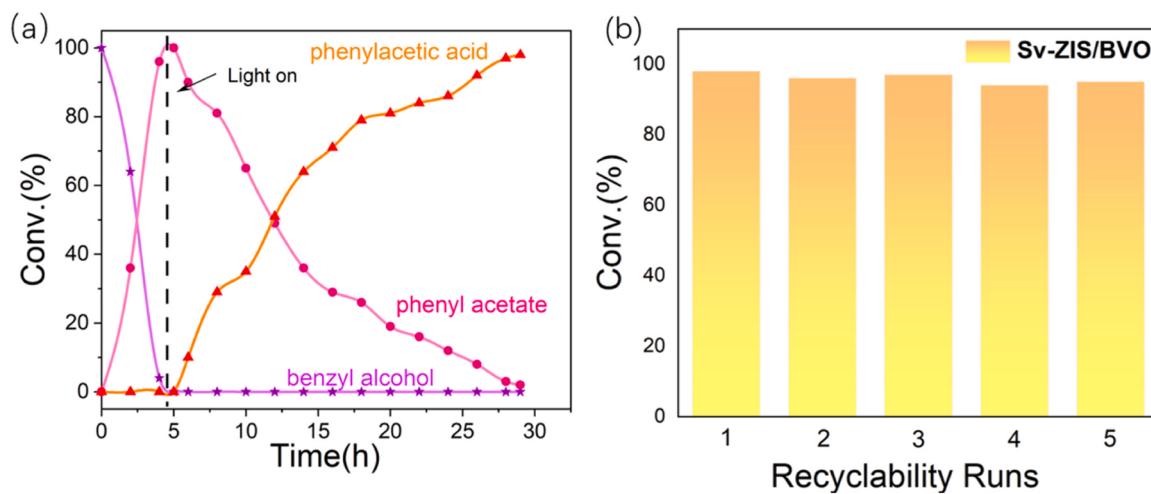

Fig. 10. (a) Kinetic curve of furfural photocatalytic carboxylation (Table 1, entry 16). (b) Recycling experiment of the photocatalyst Sv-ZIS/BVO.

homovanillic acid could be produced over the simple biomass vanillyl alcohol carboxylation with CO_2; with the consumption of 2 equivalents CO_2, the thiophene methanol and biomass platform product furfuryl alcohol could be utilized to prepare the asymmetric dicarboxylated products, which would be used as degradable polymer precursors, pharmaceutical intermediates, and cosmetics. With the Z-Scheme path migration of photogenerated electrons accelerated by internal electric field, the Z-scheme Sv-ZnIn$_2$S$_4$/BiVO$_4$ heterojunction enhanced the migration of photocarriers to promote redox capacity of photocarriers,

which could be favorable for the generation of benzylic radical and benzylic carbanion. On the other side, S vacancies enriched Sv-ZnIn$_2$S$_4$/BiVO$_4$ heterojunction further improved the photocatalytic carboxylation performance over photogenerated electrons enrichment and substrate capture ability enhancement on S vacancies. This work light up new strategy for CO_2 reutilization, biomass use and the carbon chain increased carboxylic acid production over mild heterogeneous photocatalysis.
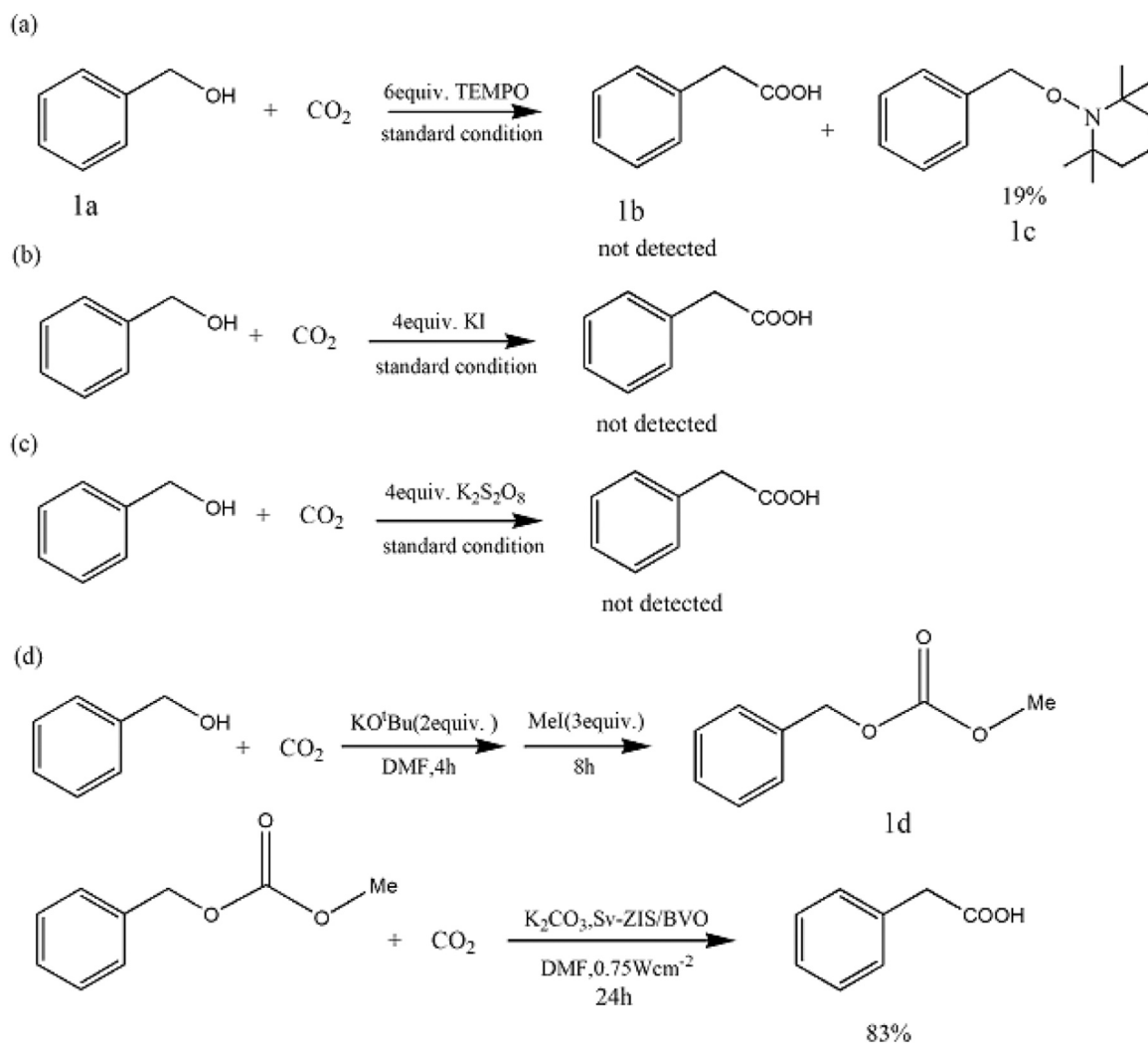
Scheme 1. Control reactions for the mechanism investigation. (a) Free radical scavenger TEMPO was introduced. (b) Hole trapping agent KI was introduced. (c) Electron scavenger $K_2S_2O_8$ was introduced. (d) Carbonate detection experiment.
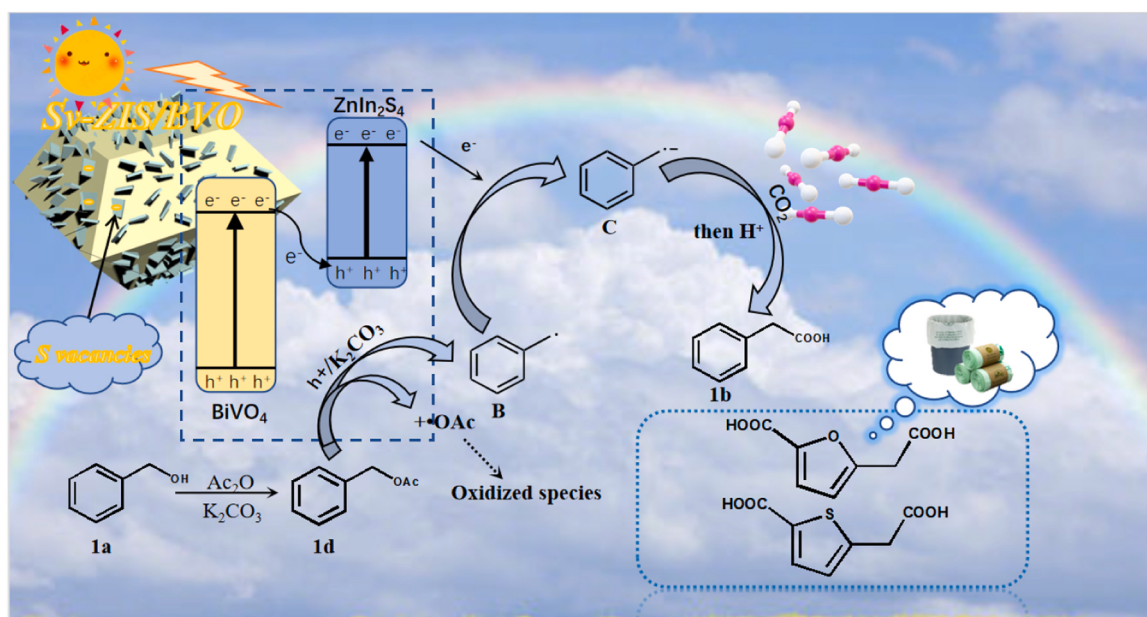
Scheme 2. Plausible reaction mechanism for the benzyl alcohol photocatalytic carboxylation with CO_2.

CRediT authorship contribution statement

Meilin Sheng: Methodology, Formal analysis, Writing-original draft, Writing-review & editing. **Chuan Gan**: Validation. **Yue Li**: Validation. **Zujie Hu**: Validation. **Qian Zhou**: Validation. **Long Qin**: Validation. **Jianmin Ren**: Supervision. **Heyan Jiang**: Supervision, Funding acquisition, Project administration.

Declaration of Competing Interest

The authors declare that they have no known competing financial interests or personal relationships that could have appeared to influence the work reported in this paper.

Data availability

No data was used for the research described in the article.

Acknowledgements

Author information

Heyan Jiang-Chongqing Key Laboratory of Catalysis and New Environmental Materials, College of Environmental and Resources, Chongqing Technology and Business University, Chongqing 400067, China; orgjiang@ 163.com. **Meilin Sheng**-Key Laboratory of Catalysis Science and Technology of Chongqing Education Commission, Chongqing Key Laboratory of Catalysis and New Environmental Materials, College of Environmental and Resources, Chongqing Technology and Business University, Chongqing 400067, China.

Associated content

Sample characterization results, experimental procedure of the photocatalytic reaction and copies of NMR spectra for all products were provided in supporting information.

Notes

The authors declare no competing financial interest.

Appendix A. Supporting information

Supplementary data associated with this article can be found in the online version at doi:10.1016/j.apcatb.2023.123138.

References

[1] L. Sullivan, A. Goryachev, I. Digdaya, X. Li, H. Atwater, D. Vermaas, C. Xiang, Coupling electrochemical CO_2 conversion with CO_2 capture, Nat. Catal. 4 (2021) 952–958.

[2] Y. Fan, J. Feng, M. Yang, X. Tan, H. Fan, M. Guo, S. Xue, CO_2 (aq) concentration–dependent CO_2 fixation via carboxylation by decarboxylase, Green. Chem. 23 (2021) 4403–4409.

[3] J. Zhang, Z. Li, Z. Zhang, K. Feng, B. Yan, Can thermocatalytic transformations of captured CO_2 reduce CO_2 emissions? Appl. Energ. 281 (2021), 116076.

[4] X. Chang, T. Wang, P. Yang, G. Zhang, J. Gong, The development of cocatalysts for photoelectrochemical CO_2 reduction, Adv. Mater. 31 (2020) 1804710.

[5] J. Guo, Y. Duan, T. Wu, W. Zhang, L. Wang, Y. Zhang, D. Wang, Atomically dispersed cerium sites in carbon-doped boron nitride for photodriven CO_2 reduction: Local polarization and mechanism insight, Appl. Catal. B 324 (2023), 122235.

[6] L. Collado, M. Gomez, M. García, F.E. Oropeza, A. Reynal, J.R. Durrant, A. Víctor, Towards the improvement of methane production in CO_2 photoreduction using Bi_2WO_6/TiO_2 heterostructures, Appl. Catal. B 324 (2023), 122206.

[7] X. He, L. Qiu, W. Wang, K. Chen, L. He, Photocarboxylation with CO_2: an appealing and sustainable strategy for CO_2 fixation, Green. Chem. 2221 (2020) 7301–7320.

[8] S. Saini, R.S. Das, A. Kumar, S.L. Jain, Photocatalytic C–H carboxylation of 1, 3-dicarbonyl compounds with carbon dioxide promoted by nickel (II)-sensitized α-Fe_2O_3 nanoparticles, ACS Catal. 12 (2022) 4978–4989.

[9] W.J. Zhou, Z.H. Wang, L.L. Liao, Y.X. Jiang, K.G. Cao, T. Ju, D.G. Yu, Reductive dearomative arylcarboxylation of indoles with CO_2 via visible-light photoredox catalysis, Nat. Commun. 11 (2020) 3263.

[10] S. Saini, H. Singh, P.K. Prajapati, A.K. Sinha, S.L. Jain, Nickel/nickel oxide in combination with a photoredox catalyst for the reductive carboxylation of unsaturated hydrocarbons with CO_2 under visible-light irradiation, ACS Sustain. Chem. Eng. 7131 (2019) 1313–11322.

[11] K. Murata, N. Numasawa, K. Shimomaki, J. Takaya, N. Iwasawa, Construction of a visible light-driven hydrocarboxylation cycle of alkenes by the combined use of Rh (I) and photoredox catalysts, Chem. Commun. 5321 (2017) 3098–3101.

[12] P. Guo, K. Wang, W.J. Jin, H. Xie, L.L. Qi, X.Y. Liu, X.Z. Shu, Dynamic kinetic cross-electrophile arylation of benzyl alcohols by nickel catalysis, J. Am. Chem. Soc. 143 (2021) 513–523.

[13] S.G. Dodekatos, H. Schünemann, Recent advances in thermo-, photo-, and electrocatalytic glycerol oxidation, ACS Catal. 87 (2018) 6301–6333.

[14] X. Liu, M. Zhang, Z. Li, CoO x-MC (MC= mesoporous carbon) for highly efficient oxidation of 5-hydroxymethylfurfural (5-HMF) to 2, 5-furandicarboxylic acid (FDCA), ACS Sustain. Chem. Eng. 812 (2020) 4801–4808.

[15] Z. Zhang, D. Shen, C. Wu, S. Gu, State-of-the-art on the production and application of carbon nanomaterials from biomass, Green. Chem. 2018 (2022) 5031–5057.

[16] J. Robinson, E. Binner, D.B. Vallejo, N.D. Perez, K. Ryan, J. Gronnow, Unravelling the mechanisms of microwave pyrolysis of biomass, Chem. Eng. J. 430 (2022) 1385–8947.

[17] G.Q. Han, X.W. Liu, Z.Y. Cao, J. Sun, Photocatalytic pinacol C-C coupling and jet fuel precursor production on $ZnIn_2S_4$ nanosheets, ACS Catal. 1016 (2020) 9346–9355.

[18] H. Wang, Y. Gao, C. Zhou, G. Li, Visible-light-driven reductive carboarylation of styrenes with CO_2 and aryl halides, J. Am. Chem. Soc. 142 (2020) 8122–8129.

[19] A. Banerjee, G. Dick, M. Kanan, Carbon dioxide utilization via carbonate-promoted C-H carboxylation, Nature 531 (2016) 215–219.

[20] M. Sheng, C. Gan, Y. Li, Z. Hu, Y. Zhang, X. Gao, H. Jiang, Photocatalytic degradable polymer precursor production and C–C bond synthesis with CO_2 over sulfur vacancies enriched $ZnIn_2S_4$ nanosheets, Chem. Eng. J. 446 (2022), 136919.

[21] Y. Zhu, L. Wang, Y. Liu, L. Shao, X. Xia, In-situ hydrogenation engineering of $ZnIn_2S_4$ for promoted visible-light water splitting, Appl. Catal. B 241 (2019) 483–490.

[22] S. Zhang, Z. Zhang, Y. Si, B. Li, F. Deng, L. Yang, S. Luo, Gradient hydrogen migration modulated with self-adapting S vacancy in copper-doped $ZnIn_2S_4$ nanosheet for photocatalytic hydrogen evolution, ACS nano 15 (2021) 15238–15248.

[23] X. Shi, L. Mao, P. Yang, H. Zheng, M. Fujitsuka, J. Zhang, Ultrathin $ZnIn_2S_4$ nanosheets with active (110) facet exposure and efficient charge separation for cocatalyst free photocatalytic hydrogen evolution, Appl. Catal. B 265 (2020), 118616.

[24] S. Meng, C. Chen, X. Gu, H. Wu, Q. Meng, J. Zhang, W. Lei, Efficient photocatalytic H_2 evolution, CO_2 reduction and N_2 fixation coupled with organic synthesis by cocatalyst and vacancies engineering, Appl. Catal. B 285 (2021), 119789.

[25] L. Wang, B. Cheng, L. Zhang, J. Yu, In situ irradiated XPS investigation on S-Scheme $TiO_2@ZnIn_2S_4$ photocatalyst for efficient photocatalytic CO_2 reduction, Small 2021 (1741) 2103447.

[26] N. Luo, T. Montini, J. Zhang, P. Fornasiero, E. Fonda, T. Hou, F. Wang, Visible-light-driven coproduction of diesel precursors and hydrogen from lignocellulose-derived methylfurans, Nat. Energy 47 (2019) 575–584.

[27] S. Song, J. Qu, P. Han, M.J. Hulsey, G. Zhang, Y. Wang, Visible-light-driven amino acids production from biomass-based feedstocks over ultrathin CdS nanosheets, Nat. Commun. 111 (2020) 4899.

[28] J. Liu, N. Ma, W. Wu, Q. He, Recent progress on photocatalytic heterostructures with full solar spectral responses, Chem. Eng. J. 393 (2020), 124719.

[29] D. Kong, X. Ruan, J. Geng, Y. Zhao, D. Zhang, X. Pu, C. Su, 0D/3D $ZnIn_2S_4/$ $Ag_6Si_2O_7$ nanocomposite with direct Z-scheme heterojunction for efficient photocatalytic H_2 evolution under visible light, Int. J. Hydrog. Energ. 46 (2021) 28043–28052.

[30] Z. Gao, K. Chen, L. Wang, B. Bai, H. Liu, Q. Wang, Aminated flower-like $ZnIn_2S_4$ coupled with benzoic acid modiffied g-C_3N_4 nanosheets via covalent bonds for ameliorated photocatalytic hydrogen generation, Cryst., Appl. Catal. B 268 (2020), 118462.

[31] X. Wang, X. Wang, J. Huang, S. Li, A. Meng, Z. Li, Interfacial chemical bond and internal electric field modulated Z-scheme S-v-$ZnIn_2S_4$/$MoSe_2$ photocatalyst for efficient hydrogen evolution, Nat. Commun. 121 (2021) 4112.

[32] C. Li, X. Du, S. Jiang, Y. Liu, Z. Niu, Z. Liu, S. Yi, X. Yue, Constructing direct Z-Scheme heterostructure by enwrapping $ZnIn_2S_4$ on CdS hollow cube for efficient photocatalytic H_2 generation, Adv. Sci. 924 (2022) 2201773.

[33] C. Du, Q. Zhang, Z. Lin, B. Yan, C. Xia, G. Yang, Half-unit-cell $ZnIn_2S_4$ monolayer with sulfur vacancies for photocatalytic hydrogen evolution, Appl. Catal. B 248 (2019) 193–201.

[34] W. Xu, W. Tian, L. Meng, F. Cao, L. Li, Interfacial chemical bond-modulated Z-Scheme charge transfer for efficient photoelectrochemical water splitting, Adv. Energy Mater. 118 (2021) 2003500.

[35] G. Zuo, Y. Wang, W. Teo, Q. Xian, Y. Zhao, Direct Z-scheme TiO_2-$ZnIn_2S_4$ nanoflowers for cocatalyst-free photocatalytic water splitting, Appl. Catal. B 291 (2021) 120126.

[36] J. Bian, J. Feng, Z. Zhang, Z. Li, Y. Zhang, Y. Liu, S. Ali, Y. Qu, L. Bai, J. Xie, D. Tang, X. Li, F. Bai, J. Tang, L. Jing, Dimension-matched zinc phthalocyanine/ $BiVO_4$ ultrathin nanocomposites for CO_2 reduction as efficient wide-visible-light-driven photocatalysts via a cascade charge transfer, Angew. Chem. Int. Ed. 58 (2019) 10873–10878.

[37] L.X. Liu, J. Fu, L.P. Jiang, J.R. Zhang, W. Zhu, Y. Lin, Highly efficient photoelectrochemical reduction of CO_2 at low applied voltage using 3D Co-Pi/ $BiVO_4/SnO_2$ nanosheet array photoanodes, ACS Appl. Mater. Inter. 11 (2019) 26024–26031.

[38] X. Shi, L. Mao, P. Yang, H. Zheng, M. Fujitsuka, J. Zhang, T. Majima, Ultrathin $ZnIn_2S_4$ nanosheets with active (110) facet exposure and efficient charge separation for cocatalyst free photocatalytic hydrogen evolution, Appl. Catal. B 265 (2020), 118616.

[39] G. Che, D. Wang, C. Wang, F. Yu, D. Li, N. Suzuki, X. Zhang, Solution plasma boosts facet-dependent photoactivity of decahedral $BiVO_4$, Chem. Eng. J. 397 (2020), 125381.

[40] J. Wang, S. Sun, R. Zhou, Y. Li, Z. He, H. Ding, W. Ao, A review: Synthesis, modification and photocatalytic applications of $ZnIn_2S_4$, J. Mater. Sci. Technol. 78 (2021) 1–19.

[41] G. Li, Q. Shen, Z. Yang, S. Kou, F. Zhang, W. Zhang, Y. Du, Photocatalytic behaviors of epitaxial $BiVO_4$ (010) thin films, Appl. Catal. B 248 (2019) 115–119.

[42] Q. Han, L. Li, W. Gao, Y. Shen, L. Wang, Y. Zhang, X. Wang, Q. Shen, Y. Xiong, Y. Zhou, Z. Zou, Elegant construction of $ZnIn_2S_4/BiVO_4$ hierarchical heterostructures as direct Z-Scheme photocatalysts for efficient CO_2 photoreduction, ACS Appl. Mater. Inter. 13 (2021) 15092–15100.

[43] S. Akrami, Y. Murakami, M. Watanabe, T. Ishihara, M. Arita, Q. Guo, K. Edalati, Enhanced CO_2 conversion on highly-strained and oxygen-deficient $BiVO_4$ photocatalyst, Chem. Eng. J. 442 (2022), 136209.

[44] S. Peng, P. Zhu, V. Thavasi, S.G. Mhaisalkar, Facile solution deposition of $ZnIn_2S_4$ nanosheet films on FTO substrates for photoelectric application, Nanoscale 3 (2011) 2602–2608.

[45] S. Zhang, X. Liu, C. Liu, S. Luo, L. Wang, T. Cai, Y. Liu, MoS_2 quantum dot growth induced by S vacancies in a $ZnIn_2S_4$ monolayer: atomic-level heterostructure for photocatalytic hydrogen production, ACS Nano 12 (2018) 751–758.

[46] Y. Gong, Y. Dong, B. Zhao, R. Yu, S. Hu, Z. Tan, Diverse applications of MoO_3 for high performance organic photovoltaics: fundamentals, processes and optimization strategies, J. Mater. Chem. A 8 (2020) 978–1009.

[47] X. Gou, F. Cheng, Y. Shi, L. Zhang, S. Peng, J. Chen, P.J. Shen, Shape-controlled synthesis of ternary chalcogenide $ZnIn_2S_4$ and $CuIn(S, Se)_2$ nano-/microstructures via facile solution route, J. Am. Chem. Soc. 128 (2006) 7222–7229.

[48] Z. Jiang, W. Wan, H. Li, S. Yuan, H. Zhao, P.K. Wong, A hierarchical Z-Scheme α-Fe_2O_3/g-C_3N_4 hybrid for enhanced photocatalytic CO_2 reduction, Adv. Mater. 30 (2018) 1706108.

[49] A. Fattah-Alhosseini, Passivity of AISI 321 stainless steel in 0.5 M H_2SO_4 solution studied by Mott-Schottky analysis in conjunction with the point defect model, Arab. J. Chem. 9 (2016) S1342–S1348.

[50] L. Li, J. Liang, L. Qin, D. Chen, Y. Huang, In situ growth of a P-type $CuSCN/Cu_2O$ heterojunction to enhance charge transport and suppress charge recombination, J. Mater. Chem. C. 7 (2019) 6872–6878.

[51] Q. Zhao, Z. Liu, Z. Guo, M. Ruan, W. Yan, The collaborative mechanism of surface S-vacancies and piezoelectric polarization for boosting CdS photoelectrochemical performance, Chem. Eng. J. 433 (2022), 133226.

[52] B. Wang, X. Wang, L. Lu, C. Zhou, Z. Xi, J. Wang, X. Ke, G.D. Sheng, S. Yan, C.Z. G. Zou, Oxygen-vacancy-activated CO_2 splitting over amorphous oxide semiconductor photocatalyst, ACS Catal. 8 (2018) 516–525.

[53] Z. Zhao, D. Wang, R. Gao, G. Wen, M. Feng, G. Song, Z. Chen, Magnetic-field-stimulated efficient photocatalytic N_2 fixation over defective $BaTiO_3$ perovskites, Angew. Chem. Int. Ed. 60 (2021) 11910–11918.

[54] Y. Qin, H. Li, J. Lu, Y. Feng, F. Meng, C. Ma, M. Meng, Synergy between van der waals heterojunction and vacancy in $ZnIn_2S_4$/g-C_3N_4 2D/2D photocatalysts for enhanced photocatalytic hydrogen evolution, Appl. Catal. B 277 (2020) 119–254.

[55] Y. Li, B. Yu, Z. Hu, H. Wang, Construction of direct Z-scheme $SnS_2@ ZnIn_2S_4@$ kaolinite heterostructure photocatalyst for efficient photocatalytic degradation of tetracycline hydrochloride, Chem. Eng. J. 429 (2022), 132105.

[56] G. Zhang, D. Chen, N. Li, Q. Xu, H. Li, J. He, J. Lu, Construction of hierarchical hollow $Co_9S_8/ZnIn_2S_4$ tubular heterostructures for highly efficient solar energy conversion and environmental remediation, Angew. Chem. Int. Ed. 132 (2020) 8332–8338.

[57] J. Estrada, S. Ramos, G. Lasarte-Aragonés, R. Lucena, S. Cárdenas, D. Rodríguez, G. Miguel, Mechanochemically designed bismuth-based halide perovskites for efficient photocatalytic oxidation of vanillyl alcohol, J. Mater. Chem. A 10 (2022) 11298–11305.

[58] S. Xu, P. Zhou, Z. Zhang, C. Yang, B. Zhang, K. Deng, H. Zhu, Selective oxidation of 5-hydroxymethylfurfural to 2, 5-furandicarboxylic acid using O_2 and a photocatalyst of Co-thioporphyrazine bonded to g-C_3N_4, J. Am. Chem. Soc. 139 (2017) 14775–14782.

[59] H. Ban, Y. Zhang, S. Chen, Y. Cheng, T. Pan, L. Wang, X. Li, Production of 2, 5-furandicarboxylic acid by optimization of oxidation of 5-methyl furfural over homogeneous Co/Mn/Br catalysts, ACS Sustain. Chem. Eng. 821 (2020) 8011–8023.

[60] A. Banerjee, G.R. Dick, T. Yoshino, M.W. Kanan, Carbon dioxide utilization via carbonate-promoted C–H carboxylation, Nature 531 (2016) 215–219.

[61] L. Buzzetti, G.E. Crisenza, P. Melchiorre, Mechanistic studies in photocatalysis, Angew. Chem. Int. Ed. 58 (2019) 3730–3747.

[62] L.L. Perissinotti, M.A. Brusa, M.A. Grela, Yield of carboxyl anion radicals in the photocatalytic degradation of formate over TiO_2 particles, Langmuir 17 (2001) 8422–8427.

[63] B. Zhang, Y. Yi, Z. Wu, Z. Chen, C. Xi, Photoredox-catalyzed dicarbofunctionalization of styrenes with amines and CO_2: a convenient access to γ-amino acids, Green. Chem. 22 (2020) 5961–5965.

[64] C. Ran, Y. Niu, L. Song, M. Wei, Y. Cao, S. Luo, D. Yu, Visible-light photoredox-catalyzed carboxylation of activated C (sp^3)-O bonds with CO_2, ACS Catal. 121 (2021) 18–24.